Efficient Electrocatalyst for the Hydrogen Evolution Reaction Derived from Polyoxotungstate/Polypyrrole/Graphene

Xiao-Li Wang, Yu-Jia Tang, Wei Huang, Chun-Hui Liu, Long-Zhang Dong, Shun-Li Li,* and Ya-Qian Lan*[a]

Efficient hydrogen evolution reaction (HER) from water by electrocatalysis using cost-effective materials is critical to realize the clean hydrogen production. Herein, with controlling the structure and composition of polyoxotungstate/conductive polypyrrole/graphene (PCG) precursor precisely and followed by a temperature-programmed reaction, we developed a highly active and stable catalyst: NC@W_xC/NRGO (NC: nitrogen-doped porous carbon, NRGO: nitrogen-doped reduced graphene oxide). The composite presents splendid performance towards HER in acidic media, with a small onset overpotential of 24 mV versus RHE (reversible hydrogen electrode), a low Tafel slope of 58.4 mV dec^{-1}, a low overpotential of 100 mV at 10 mA cm^{-2}, and remarkable long-term cycle stability. This is one of the highest HER catalysts among the tungsten carbide-based materials ever reported.

Introduction

Hydrogen, owing to its outstanding energy density and environmental friendliness, is considered to be a promising energy carrier.[1] Among various strategies to produce hydrogen, electrochemical water splitting is increasingly attractive for its suitable manufacture safety and high product purity.[2] As the cathodic reaction of electrochemical water splitting, the hydrogen evolution reaction (HER) requires a favorable catalyst to speed up the dynamics for practical application.[3] Up to date, the best HER catalysts are Pt-group metals, but the low natural abundance and high cost preclude their widespread application.[4] Therefore, it is essential to explore active noble-metal-free HER electrocatalysts to replace Pt-group metals for the realistic use of hydrogen.

In response, various types of earth-abundant electrocatalysts such as metal carbides,[5] oxides,[6] nitrides,[7] phosphides,[8] and chalcogenides[9] have been widely investigated for HER. Among these reported materials, transition metal carbides (TMCs) have received substantial attention for their low cost, high abundance, and outstanding electrochemical stability.[10] In particular, tungsten carbides have been actively studied for its platinum-like behavior since the first report by Levy and Boudart in 1973.[11] However, commercial tungsten carbides are inadequate as electrocatalysts for their inferior activities. In

recent years, considerable efforts have been devoted to improving the activity of tungsten carbides.[12] Román-Leshkov and co-workers engineered non-sintered and ultrasmall metal-terminated tungsten carbide nanoparticles to increase the active sites and improve the catalytic activity.[13] Nakanishi and co-workers reported tungsten carbonitride nanoelectrocatalysts by introducing N atom to tune the electronic state of tungsten carbides.[12b] In addition, Guo's group grew tungsten carbide nanocrystals on carbon nanotubes, which provide high surface area for the catalyst material and enhances the electron transfer for HER process.[14] Thus, engineering the structure, introducing heteroatoms, and anchoring the catalyst particles on conductive supports are effective strategies to improve the activity of tungsten carbides. Combining these strategies together, the catalytic performance of tungsten carbides could be further enhanced.

Polyoxotungstate represents a rich tungsten source and possesses high water solubility, which enable it to become a decent precursor to prepare tungsten-based catalysts.[15] Generally, tungsten carbides are prepared using a two-step strategy, including synthesis and carburization of the precursor.[14,16] However, the high temperature required to carbonize precursor easily induces uncontrollable particle sintering decreasing the amount active sites. Conductive supports can control the distribution of catalyst particles and increase the conductivity of catalysts.[15b,17] Graphene oxide (GO), as a 2D conductive support with high electrical conductivity and large specific surface area,[15b] is considered to be an ideal candidate. However, polyoxotungstate is a kind of anionic metal oxide clusters,[18] and both the GO and polyoxotungstate are negatively charged. The electrostatic repulsion between them makes it difficult to conjugate preferably.[19] To guarantee the anchoring of polyoxotungstate on GO, polypyrrole (PPy) was

[a] X.-L. Wang, Y.-J. Tang, W. Huang, C.-H. Liu, L.-Z. Dong, Prof. S.-L. Li,
Prof. Y.-Q. Lan
Jiangsu Key Laboratory of Biofunctional Materials
School of Chemistry and Materials Science
Nanjing Normal University
Nanjing 210023 (P. R. China)
E-mail: yqlan@njnu.edu.cn
slli@njnu.edu.cn

chosen to coat polyoxotungstate and load it on GO. Researchers both on theoretical calculations and experimental investigations have found that chemical doping with nitrogen atoms can tailor the electronic properties of carbon nanomaterials at the atomic scale and promote its electrocatalytic activity.[20] PPy can provide nitrogen source and dope N into GO to optimize the electronic structure and promote the electrochemical performance of the final products.
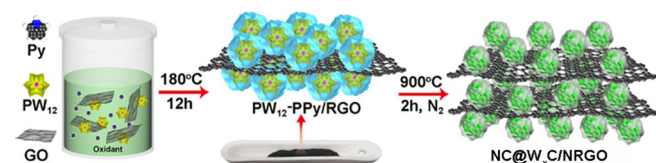
Inspired by these materials, we first synthesized the polyoxotungstate/conductive polypyrrole/graphene (denoted as PCG) precursor,[21] and obtained a novel 2D tungsten carbide-based materials by carbonizing the PCG directly. The PCG precursor with unique structure and excellent conductivity was prepared through a hydrothermal treatment for $H_3PW_{12}O_{40} \cdot n H_2O$ (PW_{12}), pyrrole monomer (Py), and GO. The final products (denoted as NC@W_xC/NRGO) is a composite consisting of N-doped reduced graphene oxide (NRGO) and tungsten carbide (WC, W_2C) nanoparticles, which are coated by N-doped porous carbon (NC). The NC@W_xC/NRGO composite exhibits extraordinary activity towards HER in 0.5 M H_2SO_4 electrolyte, giving a low onset overpotential of 24 mV versus RHE (reversible hydrogen electrode), a low Tafel slope of 58.4 mV dec^{-1}, an overpotential of 100 mV at 10 mA cm^{-2} and long-term stability. The HER performance of the composite is close to commercial Pt/C and outperforms most of the reported tungsten carbide-based materials.
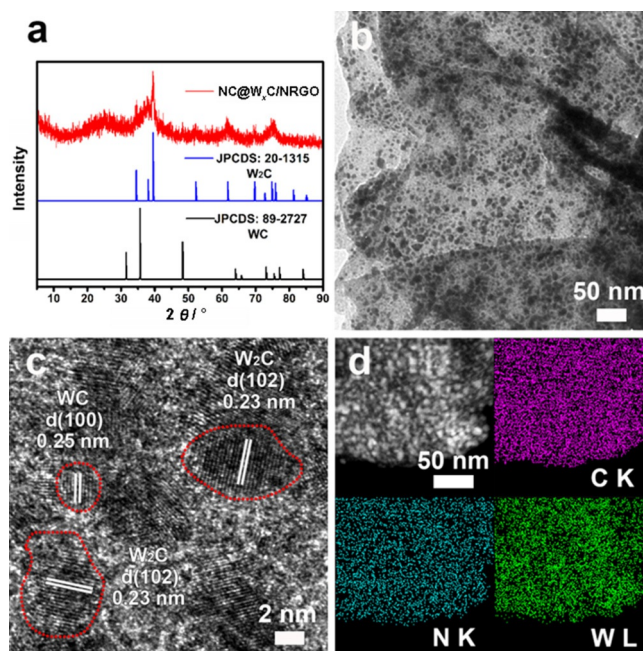
Results and Discussion

The schematic diagram for the synthesis of NC@W_xC/NRGO is shown in Scheme 1. The PW_{12}-PPy/RGO precursor was prepared using PW_{12}, Py, and GO as main raw materials by a one-pot hydrothermal method at 180 °C for 12 h. As the redox ability of PW_{12} is relatively weak, we introduced $FeCl_3 \cdot 6H_2O$ to assist PW_{12} in oxidizing Py and forming PPy. After cooling to room temperature naturally, the PW_{12}-PPy/RGO precursor was filtered, washed with a lot of deionized water, and dried at 60 °C overnight. Then the PW_{12}-PPy/RGO precursor was placed into a tubular furnace and carbonized directly in the presence of ultrapure nitrogen at 900 °C for 2 h with the heating rate of 5 °C min^{-1}. Furthermore, catalysts without the use of GO and Py were also prepared to demonstrate their critical role in enhancing the HER catalytic activity (See the Experimental Section).

The chemical composition and microstructure of the as-prepared NC@W_xC/NRGO were investigated by powder X-ray diffraction (PXRD) as displayed in Figure 1 a. The broad diffraction peak at ~25° is consistent with the (002) planes of graph-

itic carbon,[22] which derives from RGO and the porous carbon decomposed from PPy. The other peaks are indexed to W_2C (JCPDS No. 20-1315) and WC (JCPDS No. 89-2727) phases, respectively. To obtain the morphology information of the as-prepared precursor and final products, detailed microscopic characterizations were performed. Both the SEM (Figure S1 a) and TEM images (Figure S1 b) of PW_{12}-PPy/RGO demonstrate that the PW_{12}-PPy nanoparticles are loaded evenly on the RGO films. As shown in Figures 1 b and S1 c, NC@W_xC/NRGO has a similar morphology to that of the PW_{12}-PPy/RGO precursor. The highly dispersed W_xC nanoparticles with a diameter of ~3–10 nm are distributed uniformly on the NRGO films. The uniform distribution of nanoparticles both for PW_{12}-PPy/RGO and NC@W_xC/NRGO is attributed to the good water solubility of PW_{12}, which can disperse homogeneously in the GO solution. The Py monomer was oxidized and formed PPy, which was coated onto PW_{12} and then loaded uniformly onto the RGO films. Owing to the polymerization of Py, there are many wrinkled edges and a rough surface on the composite. In contrast with the morphology of PW_{12}-PPy/RGO, NC@W_xC/NRGO has a smaller particle size, which leads to the increase of active sites. When performing the same synthetic method without GO, the particles of the final products (denoted as NC@W_xC) aggregate severely (Figure S2 a, Figure S2 b), indicating the important role of GO to control the growth and distribution of W_xC nanoparticles. The SEM and TEM images of W_xC/RGO, which was prepared without the use of Py, present a similar morphology to that of NC@W_xC/NRGO (Figure S2 c,d). The high-resolution TEM (HRTEM) image of NC@W_xC/NRGO (Figure 1 c) indicates that W_xC nanoparticles are coated by NC derived from the pyrolysis of PPy. The apparent lattice fringes of

Figure 1. a) PXRD pattern of the as-prepared NC@W_xC/NRGO. b) TEM image of NC@W_xC/NRGO. c) HRTEM image of NC@W_xC/NRGO. d) STEM image of NC@W_xC/NRGO and the corresponding mapping images of C, N, and W, respectively.

Scheme 1. Preparation process of NC@W_xC/NRGO.

W$_2$C and WC can also be seen; the distance of 0.23 nm ascribes to the (102) plane of W$_2$C and the distance of 0.25 nm ascribes to the (100) plane of WC, respectively. Figure 1d presents the scanning TEM (STEM) and energy dispersive X-ray (EDX) elemental mapping images for NC@W$_x$C/NRGO. They demonstrate that C, W, and N elements distribute on NC@W$_x$C/NRGO uniformly and that N is doped into RGO. All these results confirm that the morphology control of the final products can be realized by controlling the precursor with rational composition and content.

X-ray photoelectron spectra (XPS) of NC@W$_x$C/NRGO was performed to determine its surface electronic state and elemental compositions.[23] As depicted in Figure S3a, XPS spectra of NC@W$_x$C/NRGO suggests the existence of O, C, N, W, P, and a small amount of elemental Fe in the catalyst. This result is consistent with the EDX data of NC@W$_x$C/NRGO (Figure S3b). The high-resolution XPS spectrum of C 1s (Figure S4a) shows a strong peak of C—C/C=C at 284.4 eV and two relatively weak peaks of C—N at 284.9 eV and C—O at 286.5 eV, respectively. The peak at 284.4 eV derives from the sp^2-hybridized graphitic carbon atoms, which proves the reduction of GO to RGO. The N 1s XPS spectrum (Figure S4b) demonstrates the existence of pyridinic N (397.4 eV), graphitic N (400.3 eV), and pyrrolic N (399.3 eV).[24] According to the peak area, the graphitic N is the main nitrogen species, which is related to the high carbonization temperature.[25] Figure S4c shows the high-resolution O 1s spectrum, which shows three peaks of C—O/O=C at 530.4 eV, N—C—O at 531.1 eV, and C—OH at 531.9 eV, respectively. The peak of P 2p shown in Figure 3e at 133.7 eV arises from the P—O bond (Figure S4d). The W 4f XPS spectrum (Figure S4e) shows the peaks of W 4f$_{5/2}$ at 34.8 and 37.8 eV and the peaks of W 4f$_{7/2}$ at 32.0 and 35.8 eV. The peaks at 32.0 and 34.8 eV can be assigned to tungsten carbide, whereas the peaks at 35.8 and 37.8 eV correspond to tungsten oxide, indicating the inevitable surface oxidation of tungsten carbide nanoparticles when contacted with the air.[14] Figure S4f reveals that the signal of Fe 2p is very weak, confirming that Fe has been nearly washed away.

Raman spectroscopy was investigated to further probe the structural information of NC@W$_x$C/NRGO. As seen in Figure S5, the Raman spectrum exhibits two remarkable peaks of the D band at 1352 cm^{-1} and G band at 1597 cm^{-1}. The 2D peak at around 2700 cm^{-1} is broader, demonstrating that carbonization temperature results in few-layer NRGO films.[26] The value of I_D/I_G is a major parameter to evaluate the graphitic degree of carbon materials. For NC@W$_x$C/NRGO, the value of I_D/I_G is 0.84, implying the high degree of graphitization. In addition, the Brunauer–Emmett–Teller (BET) gas absorption measurements were conducted to verify the porous nature of the main samples. Figure S6 displays the nitrogen adsorption/desorption isotherm and the corresponding pore-size distribution calculated by Barrett–Joyner–Halenda (BJH) method. The BET specific areas of NC@W$_x$C/NRGO was calculated to be 67.5 m^2 g^{-1}, which is larger than those of NC@W$_x$C (45.2 m^2 g^{-1}) and W$_x$C/RGO (58.0 m^2 g^{-1}). The corresponding pore-size distributions derived from desorption data and calculated using the BJH model shows that NC@W$_x$C/NRGO and W$_x$C/RGO are mesoporous structures with average pore sizes of ∼4 nm, whereas NC@W$_x$C has almost no pores.

The HER performance of the as-prepared electrocatalysts was investigated by depositing samples onto a glassy carbon electrode (GCE) with a catalyst loading of 0.14 mg cm^{-2} using a typical three-electrode system in 0.5 M H$_2$SO$_4$ electrolyte. Herein, all potentials were measured versus saturated calomel electrode (SCE) and presented versus reversible hydrogen electrode (RHE). For comparison, the performance of commercial 20% Pt/C, NC@W$_x$C, and W$_x$C/RGO with the same loading were also examined. The linear sweep voltammetry (LSV) curves (without iR compensation) are shown in Figure 2a. Unquestionably, the 20% Pt/C catalyst shows supreme performance, with an onset potential of nearly 0 mV.[27] Surprisingly, the as-prepared NC@W$_x$C/NRGO shows a small onset potential of only 24 mV, which is close to the value from the commercial reference sample and much smaller than the values observed for NC@W$_x$C (192 mV) and W$_x$C/RGO (174 mV). The overpotential at $j = 10$ mA cm^{-2} (η_{10}) for NC@W$_x$C/NRGO was 100 mV, much lower than that observed on NC@W$_x$C (342 mV) and W$_x$C/RGO (278 mV), and is better than those of many other reported HER electrocatalysts based on tungsten carbides (Table S1).

To elucidate the detailed mechanism of the HER activity, Tafel slopes were calculated according to the Tafel equation ($\eta = b \log j + a$), in which b is the Tafel slope and a is a constant, and presented in Figure 2b.[28] The Tafel slope for commercial 20% Pt/C was 30.2 mV dec^{-1}, which coincides with literature values.[27] For NC@W$_x$C/NRGO, the Tafel slope was 58.4 mV dec^{-1}, which is smaller than that of NC@W$_x$C (89.0 mV dec^{-1}) and W$_x$C/RGO (78.1 mV dec^{-1}), suggesting the Volmer–Heyrovsky mechanism is operative in the HER process.[8a, 29] Moreover, the value is also one of the best of electrocatalysts composed of tungsten carbides. The exchange current density (j_0) (obtained by the extrapolation method on the basic of Tafel plot) of NC@W$_x$C/NRGO was calculated to be 0.36 mA cm^{-2}, which is larger than that of NC@W$_x$C (2.58 × 10^{-3} mA cm^{-2}) and W$_x$C/RGO (3.98 × 10^{-3} mA cm^{-2}), and slightly lower than the commercial 20% Pt/C (0.44 mA cm^{-2}).

The electrochemical double-layer capacitance (C_{dl}) was calculated to estimate the electrochemical active surface area (ECSA). The NC@W$_x$C/NRGO electrocatalyst had a larger ECSA, indicating it has more active sites to speed the HER.[30] Here, the cyclic voltammetry (CV) was performed in the potential range of 0.26–0.36 V versus RHE with scan rates from 20 to 200 mV s^{-1} (Figures 2c and S7). The C_{dl} value of NC@W$_x$C/NRGO was 4.36 mF cm^{-2}, which is higher than W$_x$C@NC (1.11 mF cm^{-2}) and W$_x$C/RGO (2.12 mF cm^{-2}), suggesting that NC@W$_x$C/NRGO has more active sites. In addition, electrochemical impedance spectroscopy (EIS) measurement of the as-prepared electrocatalysts was also performed to probe the electrocatalytic kinetics on the electrode/electrolyte interface during the HER process. The Nyquist plots in Figure S8 demonstrate that NC@W$_x$C/NRGO has smaller charge transfer resistance than NC@W$_x$C and W$_x$C/RGO, which coincides with the above results.

Moreover, the catalytic stability is another importance parameter for HER catalysts to evaluate their electrocatalytic
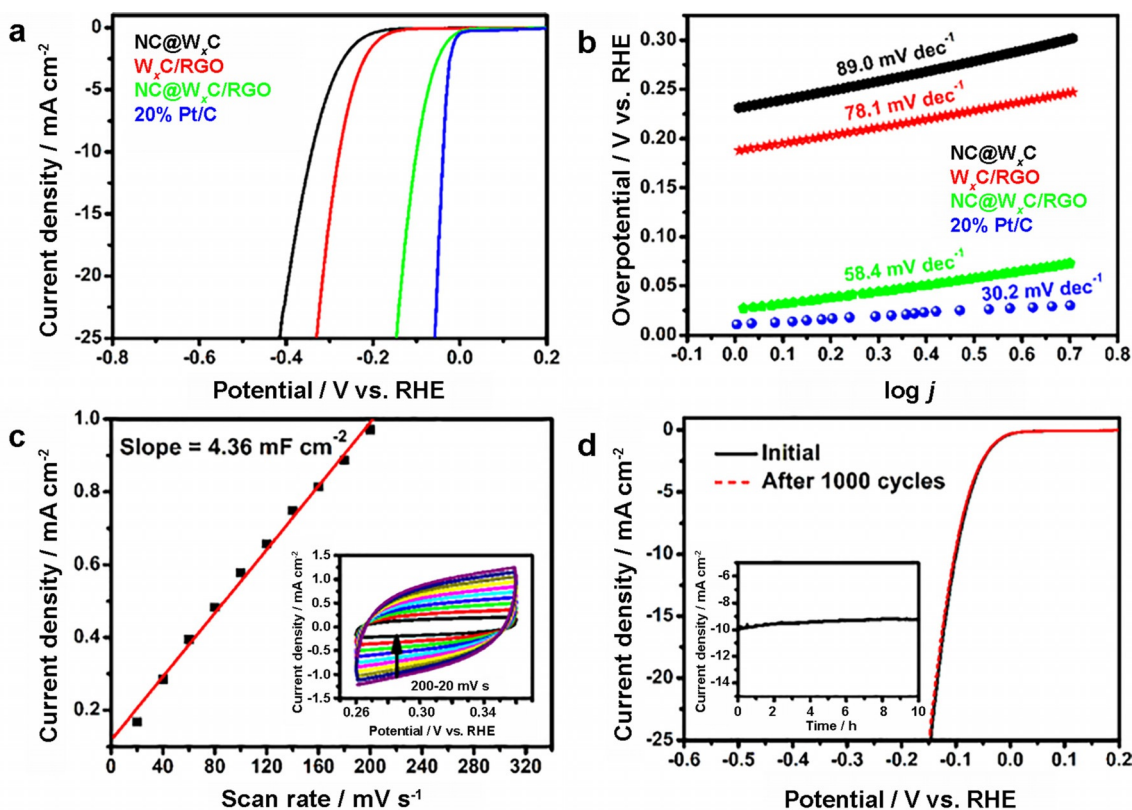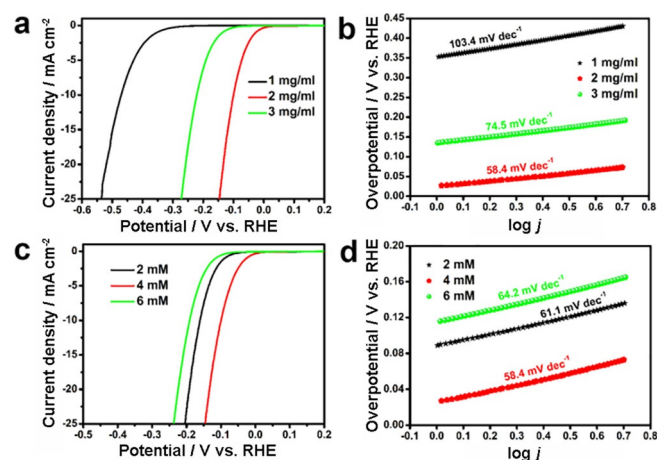
Figure 2. a) LSV curves and b) Tafel plots of NC@W$_x$C, W$_x$C/RGO, NC@W$_x$C/NRGO, and 20% Pt/C. c) Capacitive current at 0.31 V as a function of scan rate for NC@W$_x$C/NRGO (Inset: CVs of NC@W$_x$C/NRGO with different rates from 20 to 200 mV s^{-1}). d) LSV curves of NC@W$_x$C/NRGO before and after 1000 CV cycles (Inset: time-dependent current density curve of NC@W$_x$C/NRGO under a static overpotential of −350 mV vs. SCE for 10 h).

performance. To assess the durability of NC@W$_x$C/NRGO, the CV of NC@W$_x$C/NRGO was performed between −0.5 and −0.3 V at a scan rate of 100 mV s^{-1}. As shown in Figure 2 d, the LSV curve of NC@W$_x$C/NRGO exhibits nearly no difference compared with the initial one even after 1000 cycles. To further elucidate the durability of the catalyst, a chronoamperometric test of NC@W$_x$C/NRGO by electrolysis at a fixed overpotential of 350 mV was also performed (inset in Figure 2 d). This indicates that NC@W$_x$C/NRGO is stable for HER up to 10 h. These stability measurements reveal that the as-prepared NC@W$_x$C/NRGO is a highly stable electrocatalyst for HER in acidic solutions.

As comparison experiments, we prepared NC@W$_x$C/NRGO with different GO concentration, PW$_{12}$ concentration, and carbonization temperature to investigate their influence on the electrocatalytic performance. The composition and morphology of the contrast samples were studied and the HER performance was also measured using the same measurement conditions. The PXRD patterns in Figure S9 show NC@W$_x$C/NRGO (1–3 mg mL^{-1} GO) and NC@W$_x$C/NRGO (2–6 mM PW$_{12}$) have the same compositions. The performance comparison can be seen in Figure 3, NC@W$_x$C/NRGO (1 mg mL^{-1} GO) and NC@W$_x$C/NRGO (3 mg mL^{-1} GO) have poorer catalytic properties. We speculate that lower GO concentrations cannot provide enough surface area for the loading of the W$_x$C nanoparticles, whereas the higher GO concentration easily leads to aggregation and decreases the amount of active sites. The activi-

ty of NC@W$_x$C/NRGO (2 mM PW$_{12}$) and NC@W$_x$C/NRGO (6 mM PW$_{12}$) is inferior, which is attributed to the number of active sites derived from the amount of PW$_{12}$. The result is supported by the morphology presented in Figure S10: NC@W$_x$C/NRGO (2 mM PW$_{12}$) has fewer nanoparticles whereas NC@W$_x$C/NRGO (6 mM PW$_{12}$) has more, which induces inevitable aggregation of nanoparticles and decreases the active sites. In addition, the content of the tungsten source probably impacts the relative

Figure 3. a) LSV curves and b) Tafel plots of NC@W$_x$C/NRGO with different GO concentrations. c) LSV curves and d) Tafel plots of NC@W$_x$C/NRGO with different PW$_{12}$ concentrations.

compositions of WC and W_2C in the final products.[31] Catalysts prepared with 6 mM PW_{12} may possess more WC nanoparticles, which induces the relative decrease of W_2C and then decreases the catalytic performance. For different carbonization temperatures, as seen in Figures S11 and S12a, W_xC nanoparticles were not produced in abundance when carbonized at 800 °C, whereas the high temperature of 1000 °C induces sintering and aggregation of catalysts and results in poorer catalytic performance as shown in Figure S13. Therefore, the appropriate content of precursor and carbonization temperature are of great importance for preparing catalysts with high performance.

Based on all the experiments and discussion above, excellent electrocatalytic performance of $NC@W_xC/NRGO$ toward HER could be attributed to the synergistic effects among W_xC particles, NC and NRGO films. The small particle size and uniform distribution of W_xC nanoparticles contribute to the exposure of more active sites. The RGO support increases the electrical conductivity thus facilitating charge transfer in the composite. The formed NC derived from PPy could prevent the aggregation of W_xC particles. Besides, PPy can provide the nitrogen source and dope it into RGO films, which can optimize the electronic structure of the composite and lead to better activity. All these factors indicate that using PCG as precursor plays an important role for preparing $NC@W_xC/NRGO$ with extraordinary HER performance.

Conclusions

We synthesized new tungsten carbide composites derived from polyoxotungstate/conductive polypyrrole/graphene (PCG) precursors by a facile hydrothermal treatment and temperature-programmed reaction. The $NC@W_xC/NRGO$ composite exhibits an excellent activity for the hydrogen evolution reaction (HER) in the acidic electrolyte, with a low onset overpotential of 24 mV versus RHE, Tafel slope of 58.4 mV dec^{-1}, η_{10} of 100 mV (overpotential at 10 mA cm^{-2}) and good stability. The performance outperforms most of the reported tungsten carbide-based catalysts. The present work could be extended to synthesize other 2D polyoxometalate-based precursors and further obtain other tungsten-based catalysts such as tungsten nitrides, tungsten phosphides, tungsten oxides, and tungsten sulfides.

Experimental Section

Materials: Natural graphite powder was purchased from Aladdin. Potassium permanganate (KMnO$_4$, $\geq$99%), hydrogen peroxide (H$_2$O$_2$, 30%), hydrochloric acid (HCl, 36%), concentrated sulfuric acid (H$_2$SO$_4$, 98%), phosphotungstic acid (H$_3$PW$_{12}$O$_{40}$·nH$_2$O), and iron(III) chloride hexahydrate (FeCl$_3$·6H$_2$O) were purchased from Sinopharm Chemical Reagent Co. Ltd. Phosphorus(V) oxide (P$_2$O$_5$, $\geq$98.0%) and potassium persulfate (K$_2$S$_2$O$_8$, $\geq$99.5%) were purchased from Shanghai lingfeng Chemical Reagent Co. Ltd. Pyrrole (C$_4$H$_5$N, $\geq$98.0%) was purchased from Shanghai kefeng Industry& Commerce Co. Ltd. Nafion solution (5 wt%) was purchased from Sigma–Aldrich. All chemicals were purchased and used without further purification. The water used in the experiments was Millipore water (18.25 MΩ).

Synthesis of GO: GO was pre-synthesized using a modified Hummers method.[32]

Synthesis of PW$_{12}$-PPy/RGO: PW$_{12}$-PPy/RGO was synthesized by a one-pot hydrothermal method. Briefly, GO (80 mg) was dispersed in deionized water (30 mL) by ultrasonication to form a homogeneous solution. Then, PW$_{12}$ (0.4608 g, 4 mM) and FeCl$_3$·6H$_2$O (0.5406 g, 2 mmol) were added into the above solution, followed by mixing it with Py (69 μL, 1 mmol), which was dissolved in deionized water (10 mL). Subsequently, the solution was transferred into a 50 mL Teflon-lined stainless steel autoclave, sealed and maintained at 180 °C for 12 h. After cooling down to room temperature naturally, the as-synthesized material (denoted as PW$_{12}$-PPy/RGO) was filtered, washed with deionized water repeatedly, dried at 60 °C overnight, and grounded into powder for heat treatment. Herein, the concentration of GO is 2 mg mL^{-1}, the concentration of PW$_{12}$ is 4 mM, the carbonization temperature is 900 °C, except where noted.

Synthesis of NC@W$_x$C/NRGO: To obtain NC@W$_x$C/NRGO, the PW$_{12}$-PPy/RGO powder was placed into a tubular furnace and carbonized in the presence of ultrapure N$_2$ at 900 °C for 2 h with a heating rate of 5 °C min^{-1}. For comparison, NC@W$_x$C/NRGO with different GO concentrations (1–3 mg mL^{-1}), different PW$_{12}$ concentrations (2 mM–6 mM), and different carbonization temperatures (800 °C–1000 °C) were also synthesized. The synthesis methods were similar to that used for NC@W$_x$C/NRGO, except the concentration and carbonization temperature.

Synthesis of NC@W$_x$C: NC@W$_x$C was synthesized without adding GO by the same procedure that was used for NC@W$_x$C/NRGO.

Synthesis of W$_x$C/RGO: W$_x$C/RGO was synthesized without adding Py monomers by the same procedure that was used for NC@W$_x$C/NRGO.

Characterizations: PXRD patterns were collected on a D/max 2500 VL/PC diffractometer (Japan) equipped with graphite monochromatized CuK$_\alpha$ radiation ($\lambda = 1.54060$ Å). Corresponding work voltage and current density was 40 kV and 100 mA, respectively. The morphology and structure of the samples were analyzed by SEM (JEOL-2100F) with an acceleration voltage of 10 kV and TEM (JEM-200CX) with an acceleration voltage of 200 kV. High-resolution TEM (HRTEM) imaging was performed on FEI Tecnai G2 F30 apparatus with an accelerating voltage of 300 kV. Elemental mapping and EDX were taken on JSM-5160LV-Vantage typed energy spectrometer. XPS was performed on scanning X-ray microprobe (PHI 5000 Versasa, ULAC-PHI, Inc.) using AlK$_\alpha$ radiation and the C1s peak at 284.8 eV as internal standard. The Raman measurement was performed on Lab-RAM HR800 with a laser excitation wavelength of 514.5 nm. The nitrogen adsorption/desorption was determined by Quantachrome Instruments Autosorb AS-6B at 77 K. The pore-size distributions were measured by the Barrett–Joyner–Halenda (BJH) method.

Electrocatalytic Measurements: All electrocatalytic activity measurements of the as-synthesized catalysts were performed at ambient environment on the CHI Instruments 660e electrochemical workstation (Shanghai Chenhua Co. Ltd., China) in a standard three-electrode system. Glassy carbon electrode (GCE, 3 mm in diameter), Pt wire, and saturated calomel electrode (SCE, saturated KCl-filled) were used as the working electrode, the auxiliary electrode, and the reference electrode, respectively. A flow of N$_2$ was bubbled through the electrolyte for at least 30 minutes prior to

electrochemical treatment and kept on during measurements. The potential was measured versus SCE and presented versus RHE. The potential conversion was based on the Nernst equation: E [V vs. RHE] $= E$ [V vs. SCE] $+ 0.2415$ V $+ 0.0591 \times$ pH. The sample was prepared by dispersing the catalyst (4 mg) into 9:1 v/v water/Nafion (2 mL) by ultrasonication to form a homogeneous ink. Then 5 μL of the ink was covered onto a GCE (loading amount of ≈ 0.14 mg cm^{-2}) and dried at room temperature for measurements. Commercial 20% Pt/C catalyst was used as a reference sample. The polarization curves were recorded by LSV mode at a scan rate of 5 mV s^{-1}. EIS measurement was performed from 1000 kHz to 100 mHz with an amplitude of 10 mV at open-circuit voltage. The long-term stability of the catalyst was evaluated by cycling the potential between -0.5 and -0.3 V vs. SCE at a scan rate of 100 mV s^{-1}. To evaluate the ECSA of the catalyst, CV was used for measuring the double-layer capacitance (C_{dl}) under the potential window of 0.015–0.115 V vs. SCE with various scan rates from 20–200 mV s^{-1}. All polarization curves were obtained without iR compensation.

Acknowledgements

[1] a) Y. Jiao, Y. Zheng, M. Jaroniec, S. Z. Qiao, *Chem. Soc. Rev.* **2015**, *44*, 2060–2086; b) J. A. Turner, *Science* **2004**, *305*, 972–974.

[2] a) T. R. Cook, D. K. Dogutan, S. Y. Reece, Y. Surendranath, T. S. Teets, D. G. Nocera, *Chem. Rev.* **2010**, *110*, 6474–6502; b) A. I. Hochbaum, P. Yang, *Chem. Rev.* **2010**, *110*, 527–546; c) T. Liu, Q. Liu, A. M. Asiri, Y. Luo, X. Sun, *Chem. Commun.* **2015**, *51*, 16683–16686.

[3] a) J. Jiang, M. Gao, W. Sheng, Y. Yan, *Angew. Chem. Int. Ed.* **2016**, *55*, 15240–15245; *Angew. Chem.* **2016**, *128*, 15466–15471; b) T. Liu, Y. Liang, Q. Liu, X. Sun, Y. He, A. M. Asiri, *Electrochem. Commun.* **2015**, *60*, 92–96.

[4] a) C. G. Morales-Guio, L.-A. Stern, X. Hu, *Chem. Soc. Rev.* **2014**, *43*, 6555–6569; b) M. S. Faber, S. Jin, *Energy Environ. Sci.* **2014**, *7*, 3519–3542; c) X. Zou, Y. Zhang, *Chem. Soc. Rev.* **2015**, *44*, 5148–5180.

[5] Y. Zhao, K. Kamiya, K. Hashimoto, S. Nakanishi, *J. Am. Chem. Soc.* **2015**, *137*, 110–113.

[6] R. Wu, J. Zhang, Y. Shi, D. Liu, B. Zhang, *J. Am. Chem. Soc.* **2015**, *137*, 6983–6986.

[7] J. Xie, S. Li, X. Zhang, J. Zhang, R. Wang, H. Zhang, B. Pan, Y. Xie, *Chem. Sci.* **2014**, *5*, 4615–4620.

[8] a) P. Xiao, M. A. Sk, L. Thia, X. Ge, R. J. Lim, J.-Y. Wang, K. H. Lim, X. Wang, *Energy Environ. Sci.* **2014**, *7*, 2624–2629; b) C. Tang, R. Zhang, W. Lu, L. He, X. Jiang, A. M. Asiri, X. Sun, *Adv. Mater.* **2017**, *29*, 1602441–1602446.

[9] D. Voiry, H. Yamaguchi, J. Li, R. Silva, D. C. B. Alves, T. Fujita, M. Chen, T. Asefa, V. B. Shenoy, G. Eda, M. Chhowalla, *Nat. Mater.* **2013**, *12*, 850–855.

[10] W.-F. Chen, J. T. Muckerman, E. Fujita, *Chem. Commun.* **2013**, *49*, 8896–8909.

[11] R. B. Levy, M. Boudart, *Science* **1973**, *181*, 547–549.

[12] a) W.-F. Chen, J. M. Schneider, K. Sasaki, C.-H. Wang, J. Schneider, S. Iyer, S. Iyer, Y. Zhu, J. T. Muckerman, E. Fujita, *ChemSusChem* **2014**, *7*, 2414–2418; b) Y. Zhao, K. Kamiya, K. Hashimoto, S. Nakanishi, *Angew. Chem. Int. Ed.* **2013**, *52*, 13638–13641; *Angew. Chem.* **2013**, *125*, 13883–13886; c) S. T. Hunt, T. M. Kokumai, D. Zanchet, Y. Román-Leshkov, *J. Phys. Chem. C* **2015**, *119*, 13691–13699; d) Y. N. Regmi, B. M. Leonard, *Chem. Mater.* **2014**, *26*, 2609–2616.

[13] S. T. Hunt, T. Nimmanwudipong, Y. Román-Leshkov, *Angew. Chem. Int. Ed.* **2014**, *53*, 5131–5136; *Angew. Chem.* **2014**, *126*, 5231–5236.

[14] X. Fan, H. Zhou, X. Guo, *ACS Nano* **2015**, *9*, 5125–5134.

[15] a) D.-Y. Du, J.-S. Qin, S.-L. Li, Z.-M. Su, Y.-Q. Lan, *Chem. Soc. Rev.* **2014**, *43*, 4615–4632; b) H. Yan, C. Tian, L. Wang, A. Wu, M. Meng, L. Zhao, H. Fu, *Angew. Chem. Int. Ed.* **2015**, *54*, 6325–6329; *Angew. Chem.* **2015**, *127*, 6423–6427.

[16] a) Q. Gong, Y. Wang, Q. Hu, J. Zhou, R. Feng, P. N. Duchesne, P. Zhang, F. Chen, N. Han, Y. Li, C. Jin, Y. Li, S.-T. Lee, *Nat. Commun.* **2016**, *7*, 13216; b) Y. Zhou, R. Ma, P. Li, Y. Chen, Q. Liu, G. Cao, J. Wang, *J. Mater. Chem. A* **2016**, *4*, 8204–8210; c) S. Bukola, B. Merzougui, A. Akinpelu, M. Zeama, *Electrochim. Acta* **2016**, *190*, 1113–1123.

[17] J.-S. Li, Y. Wang, C.-H. Liu, S.-L. Li, Y.-G. Wang, L.-Z. Dong, Z.-H. Dai, Y.-F. Li, Y.-Q. Lan, *Nat. Commun.* **2016**, *7*, 11204.

[18] B. Nohra, H. El Moll, L. M. Rodriguez Albelo, P. Mialane, J. Marrot, C. Mellot-Draznieks, M. O'Keeffe, R. Ngo Biboum, J. Lemaire, B. Keita, L. Nadjo, A. Dolbecq, *J. Am. Chem. Soc.* **2011**, *133*, 13363–13374.

[19] D. Zhou, B.-H. Han, *Adv. Funct. Mater.* **2010**, *20*, 2717–2722.

[20] W. J. Lee, J. Lim, S. O. Kim, *Small Methods* **2017**, *1*, 1600014.

[21] C.-H. Liu, Y.-J. Tang, X.-L. Wang, W. Huang, S.-L. Li, L.-Z. Dong, Y.-Q. Lan, *J. Mater. Chem. A* **2016**, *4*, 18100–18106.

[22] W. Zhou, J. Zhou, Y. Zhou, J. Lu, K. Zhou, L. Yang, Z. Tang, L. Li, S. Chen, *Chem. Mater.* **2015**, *27*, 2026–2032.

[23] Z. Pu, Q. Liu, A. M. Asiri, X. Sun, *ACS Appl. Mater. Interfaces* **2014**, *6*, 21874–21879.

[24] a) R. Ma, Y. Zhou, Y. Chen, P. Li, Q. Liu, J. Wang, *Angew. Chem. Int. Ed.* **2015**, *54*, 14723–14727; *Angew. Chem.* **2015**, *127*, 14936–14940; b) J. Duan, S. Chen, M. Jaroniec, S. Z. Qiao, *ACS Nano* **2015**, *9*, 931–940.

[25] Z.-H. Sheng, L. Shao, J.-J. Chen, W.-J. Bao, F.-B. Wang, X.-H. Xia, *ACS Nano* **2011**, *5*, 4350–4358.

[26] a) H. S. S. Ramakrishna Matte, A. Gomathi, A. K. Manna, D. J. Late, R. Datta, S. K. Pati, C. N. R. Rao, *Angew. Chem. Int. Ed.* **2010**, *49*, 4059–4062; *Angew. Chem.* **2010**, *122*, 4153–4156; b) C. H. Lui, L. Liu, K. F. Mak, G. W. Flynn, T. F. Heinz, *Nature* **2009**, *462*, 339–341; c) J.-S. Li, S.-L. Li, Y.-J. Tang, M. Han, Z.-H. Dai, J.-C. Bao, Y.-Q. Lan, *Chem. Commun.* **2015**, *51*, 2710–2713.

[27] Y. Li, H. Wang, L. Xie, Y. Liang, G. Hong, H. Dai, *J. Am. Chem. Soc.* **2011**, *133*, 7296–7299.

[28] Z. Xing, Q. Liu, A. M. Asiri, X. Sun, *ACS Catal.* **2015**, *5*, 145–149.

[29] a) T. F. Jaramillo, K. P. Jørgensen, J. Bonde, J. H. Nielsen, S. Horch, I. Chorkendorff, *Science* **2007**, *317*, 100–102; b) C. Tang, L. Gan, R. Zhang, W. Lu, X. Jiang, A. M. Asiri, X. Sun, J. Wang, L. Chen, *Nano Lett.* **2016**, *16*, 6617–6621.

[30] M. A. Lukowski, A. S. Daniel, F. Meng, A. Forticaux, L. Li, S. Jin, *J. Am. Chem. Soc.* **2013**, *135*, 10274–10277.

[31] D. J. Ham, R. Ganesan, J. S. Lee, *Int. J. Hydrogen Energy* **2008**, *33*, 6865–6872.

[32] J. H. Lee, N. Park, B. G. Kim, D. S. Jung, K. Im, J. Hur, J. W. Choi, *ACS Nano* **2013**, *7*, 9366–9374.